CHEMISTRY OF MATERIALS

pubs.acs.org/cm

Article

Solvent-Mediated Synthesis of Amorphous Li_3PS_4/Polyethylene Oxide Composite Solid Electrolytes with High Li^+ Conductivity

Ethan C. Self,*,# Zachary D. Hood,*,# Teerth Brahmbhatt, Frank M. Delnick, Harry M. Meyer, III, Guang Yang, Jennifer L. M. Rupp, and Jagjit Nanda*

Cite This: *Chem. Mater.* 2020, 32, 8789–8797

Read Online

ACCESS | Metrics & More | Article Recommendations | Supporting Information

ABSTRACT: Solvent-mediated routes have emerged as an effective, scalable, and low-temperature method to fabricate sulfide-based solid-state electrolytes. However, tuning the synthesis conditions to optimize the electrolyte's morphology, structure, and electrochemical properties is still underexplored. Here, we report a new class of composite solid electrolytes (SEs) containing amorphous Li_3PS_4 synthesized in situ with a poly(ethylene oxide) (PEO) binder using a one-pot, solvent-mediated route. The solvent and thermal processing conditions have a dramatic impact on the Li_3PS_4 structure. Conducting the synthesis in tetrahydrofuran resulted in crystalline β-Li_3PS_4 whereas acetonitrile led to amorphous Li_3PS_4. Annealing at 140 °C increased the Li^+ conductivity of an amorphous composite (Li_3PS_4 + 1 wt % PEO) by 3 orders of magnitude (e.g., from 4.5×10^{-9} to 8.4×10^{-6} S/cm at room temperature) because of: (i) removal of coordinated solvent and (ii) rearrangement of the polyanionic network to form $P_2S_7^{4-}$ and PS_4^{3-} moieties. The PEO content in these composites should be limited to 1−5 wt % to ensure reasonable Li^+ conductivity (e.g., up to 1.1×10^{-4} S/cm at 80 °C) while providing enough binder to facilitate scalable processing. The results of this study highlight a new strategy to suppress crystallization in sulfide-based SEs,, which has important implications for solid-state batteries.

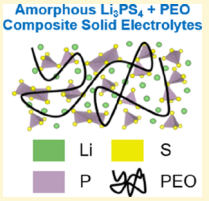

INTRODUCTION

A critical challenge for Li-based solid-state batteries (SSBs) is the development of solid electrolytes (SEs) that exhibit: (i) high Li^+ conductivity comparable to that of liquid organic electrolytes and (ii) good electrochemical and mechanical compatibility with Li metal anodes and high energy density cathodes.[1] Nanocrystalline β-Li_3PS_4 represents a promising SE candidate because of its high ionic conductivity (1.5×10^{-4} S/cm at room temperature),[2−4] but a major bottleneck for this material and related sulfide-based SEs is the lack of scalable processing methods to produce films <30 μm thick, which are critical for high energy density SSBs.[2] Furthermore, the nano−/polycrystalline structure of many SEs may cause nonuniform current densities and unstable Li growth during battery operation.[5] In comparison, amorphous SEs which lack distinct grain boundaries may promote more uniform Li plating/stripping and therefore may improve long-term cycling in full cells.[6−11]

Sulfide-based SE powders are typically synthesized using either: (i) high temperature mechanochemical and solid state methods or (ii) solvent-mediated routes in which the precursors (e.g., Li_2S and P_2S_5) are dispersed in an organic solvent (e.g., tetrahydrofuran (THF), acetonitrile (AN), or ethyl acetate) followed by drying and thermal annealing.[12−15] The latter approach has been used to fabricate a wide range of Li-P-S ternary crystalline compounds (e.g., β-Li_3PS_4, $Li_7P_3S_{11}$, and Li_7PS_6)[2−4,16] and metal/halide-substituted materials (e.g., $0.4LiX\bullet0.6Li_4SnS_4$ and Li_6PS_5X, X = Cl, Br, I)[12,13,17−20] with Li^+ conductivities ≥1×10^{-4} S/cm at room temperature. As detailed in prior reviews,[12−14,21] solvent-mediated synthesis leads to products with structures and electrochemical properties, which are greatly dependent on the composition, solvent, mixing protocol, and thermal post-treatment.

The Li^+ conductivity of sulfide-based SEs is closely linked to the material's microstructure and local Li bonding environments.[22] With respect to crystalline Li_3PS_4, two phases exist at room temperature, namely, the bulk γ phase and the nanostructured β phase. Simulations suggest that the higher Li^+ conductivity of β-Li_3PS_4 is due to the high anisotropic diffusion rates of interstitial Li^+ along the [100], [010], and [001] directions compared to γ-Li_3PS_4.[23] Furthermore, nudged elastic band calculations reported by Holzwarth and coworkers indicate that the formation of vacancy-interstitial pairs gives rise to superionic conductivities in β-Li_3PS_4.[24] On the other hand, simulations based on the Nernst−Einstein relationship of amorphous Li_2S-P_2S_5 glasses indicate an interplay between the Li^+ diffusivity and concentration, whereas isolated sulfur suppresses Li^+ migration.[25] Though the Li^+ conduction mechanism varies significantly throughout Li-P-S systems, less is generally known about amorphous and glass-type ion conductors.

Received: May 11, 2020
Revised: September 18, 2020
Published: September 21, 2020

https://dx.doi.org/10.1021/acs.chemmater.0c01990
Chem. Mater. 2020, 32, 8789−8797

To develop Li-based SSBs with energy densities >350 Wh/kg, the SE layer should be <30 μm thick to compete with traditional LIBs using polymer separators.[26−28] If made sufficiently thin, even SEs with modest conductivities yield acceptable area-specific resistances for some applications (e.g., 50 Ω cm^2 for a 5 μm thick SE layer with an ionic conductivity of 1 × 10^{-5} S/cm). Operating SSBs at elevated temperatures (≥60 °C, not readily accessible to conventional Li-ion systems) would further decrease the area-specific resistance. However, because of difficulties in producing scalable thin film ceramics, most SSB research utilizes SE pellets (ca. 0.5−1 mm thick) in which the SE occupies a large mass and volume fraction of the cell. This limitation can potentially be resolved by developing composite SEs that contain: (i) a sulfide-based superionic conductor to attain suitable Li^+ conductivity and (ii) a polymer component to improve material processability. A wide range of composite polymer/inorganic SEs have been reported[29−39] with comprehensive reviews given in references.[40−42] In these studies, several processing and synthesis methods have been employed including: (i) casting slurries containing a polymer electrolyte and preannealed ceramic particles, (ii) backfilling polymer electrolytes into porous ceramic templates, (iii) blending polymer and sulfide electrolyte precursors in a single slurry, and (iv) modifying the ceramic's surface chemistry to improve compatibility with the polymer electrolyte. Particularly relevant to the present work, Chen et al.[29] reported an SE containing a Li^+ conducting polymer [poly(ethylene oxide) (PEO) + lithium bis(trifluoromethanesulfonyl)imide, PEO + LiTFSI] and a β-Li_3PS_4 filler (1−5 vol.%) to reduce the crystallinity of the PEO + LiTFSI phase. Notably, β-Li_3PS_4 was synthesized in the presence of the polymer electrolyte through a one-pot method. Because of the high volume fraction of the polymer, Li^+ conduction occurred primarily through the polymer matrix. To the best of our knowledge, the effects of the higher Li_3PS_4 content on the structure and Li^+ conductivity of these composites were not explored.

The present work describes the one-pot synthesis of a new class of amorphous Li_3PS_4/PEO composite SEs in which the PEO serves as a binder to improve material processability. Here, the Li_3PS_4 is synthesized in situ by blending the Li_2S, P_2S_5, and PEO in AN followed by thermal annealing (see Figure 1). AN is completely removed after thermally annealing the electrolyte at 140−250 °C while the polymer remains and plays a key role in predefining the spacing between $P_2S_7^{4-}$ and PS_4^{3-} moieties. This approach enables the production of a wide range of composites in which the Li^+-conducting phase (Li_3PS_4) is intimately blended with the polymer binder (PEO). The effects of different solvents and heat treatments on the phase and micro/nanostructure evolution of the composite electrolytes were evaluated using X-ray diffraction (XRD), cryogenic transmission electron microscopy (cryo-TEM), Raman spectroscopy, and X-ray photoelectron spectroscopy (XPS). Through this work, we provide a new synthesis protocol and clarify how PEO incorporation into the composite acts as a network former, with regard to the $P_2S_7^{4-}$/PS_4^{3-} moieties and interstitial Li^+ in the structure. These findings are combined with Li^+ conductivity measurements to establish structure/transport correlations for this new class of amorphous sulfide-based SEs.

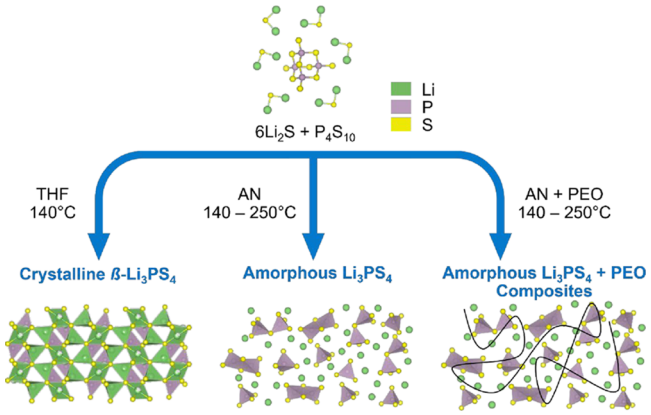

Figure 1. Schematic illustrating the solvent-mediated synthesis of Li_3PS_4 and Li_3PS_4/PEO composite SEs in this study. Although the synthesis in THF led to the formation of crystalline β-Li_3PS_4 after heating at 140 °C, syntheses performed in AN resulted in amorphous Li_3PS_4 after heating to 140−250 °C. In situ synthesis of Li_3PS_4 in the presence of PEO enables the production of a wide range of composites in which the Li^+ conducting phase (Li_3PS_4) is intimately blended with the polymer binder (PEO). THF, AN, and PEO denote THF, acetonitrile, and poly(ethylene oxide), respectively.

RESULTS AND DISCUSSION

Li_3PS_4 powders were synthesized through a solvent-mediated route in which Li_2S and P_2S_5 were mixed in either THF or AN. When prepared in THF, the powders dried at room temperature contained the cocrystallized solvent (denoted Li_3PS_4•3THF), which was removed by heating to 140 °C to yield crystalline β-Li_3PS_4 (see Figure S1). On the other hand, syntheses conducted in AN led to an amorphous Li_3PS_4 product (see Figure 2), which contained weak reflections

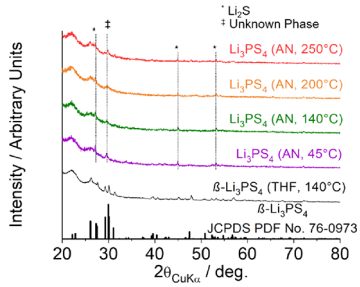

Figure 2. Powder XRD patterns of Li_3PS_4 prepared using THF and AN solvents and annealed at 45−250 °C. The broad background at 20−30 ° is due to the Kapton film, which was used to mitigate air exposure during the measurements. Syntheses conducted in THF resulted in crystalline β-Li_3PS_4 whereas using AN resulted in an amorphous Li_3PS_4 phase.

indexed to trace Li_2S and a broad peak at 2θ ~29.6 ° (full width at half maximum ~0.6° compared to ~0.2° for β-Li_3PS_4, see Figure 2). Interestingly, heating this amorphous Li_3PS_4 at 140−250 °C for ≥12 h did not induce crystallization of the expected β-Li_3PS_4 phase as reported in the literature.[3,29,43] Instead, the material thermally decomposed at temperatures ≥200 °C as evidenced by gray discoloration of the powder and formation of a gray film, which condensed outside the furnace's heating zone. The discrepancy between our work and previous studies is attributed to subtle differences in the experimental protocols (e.g., mixing methodology, annealing time, and atmosphere) and thus the formation of different AN-

https://dx.doi.org/10.1021/acs.chemmater.0c01990
Chem. Mater. 2020, 32, 8789−8797

coordinated intermediates, which underwent unique reaction pathways upon thermal annealing. We speculate that this amorphous Li_3PS_4, which lacks discrete crystalline grains (shown later using cryo-TEM), may be useful to mitigate unstable Li growth in SSBs.

Developing composite SEs containing the Li_3PS_4 + polymer binder is one way to facilitate processing of thin SE layers for high energy SSBs. As such, the primary focus of this work is on the development of new amorphous Li_3PS_4/ PEO composites in which the Li_3PS_4 is synthesized in the presence of PEO binder, resulting in an intimate blend of the two components. The impact of PEO incorporation on the phase and microstructure of the SEs was evaluated by XRD, scanning electron microscopy (SEM), energy-dispersive X-ray spectroscopy (EDS), and cryo-TEM. Figure 3 shows that the XRD

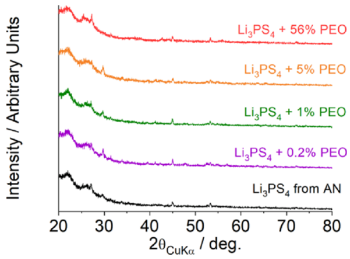

Figure 3. Powder XRD patterns of Li_3PS_4 and Li_3PS_4 + PEO composites containing 0.2−56 wt % PEO prepared using AN and annealed overnight at 140 °C. Amorphous Li_3PS_4 + PEO composites had similar structures compared to amorphous Li_3PS_4 obtained from AN.

patterns of Li_3PS_4 + PEO composites containing 0.2−56 wt % PEO were very similar to that of amorphous Li_3PS_4 prepared from AN. Interestingly, while pure PEO exhibited a sharp peak at 2θ = ∼24 ° (see Figure S2) because of the polymer's semicrystalline structure at room temperature,[44] this peak was absent for the PEO-containing composites. This finding indicates that PEO crystallinity was greatly suppressed in the composites, possibly because of coordination between Li_3PS_4 and the polymer's ether functional group. Figures S3 and S4 show SEM and EDS analyses of cold-pressed pellets containing 1 and 56 wt % PEO. The Li_3PS_4 + 1% PEO composite contained some visible surface pores, and a higher PEO content promoted a significantly smoother surface. EDS maps of these pellets showed a homogeneous distribution of C, O, P, and S, which indicates that the one-pot synthesis promotes good contact between Li_3PS_4 and PEO.

TEM was employed to further probe: (i) the contact between the Li_3PS_4 and PEO and (ii) nanocrystalline domains which may exist in these amorphous materials. Lithium thiophosphates are notoriously difficult to study via TEM at room temperature because of their high beam sensitivity.[45,46] Therefore, this study utilized cryo-TEM (holder cooled by liquid nitrogen) and low electron dose fluxes (<1000 e^- $Å^{-2}$ s^{-1}) to minimize beam damage. Figure 4a and b show representative cryo-TEM images of Li_3PS_4 + PEO composites containing 1 and 56 wt % polymer, respectively. The composites were almost entirely amorphous with no detectable nanocrystalline β-Li_3PS_4. However, these samples contained small domains (<50 nm) associated with: (i) crystalline Li_2S (see fast-Fourier transform (FFT) in Figure 4a) and (ii) PEO crystallites (d-spacing ∼2 nm) because of the low temperature of the cryogenic holder, which was well below the glass

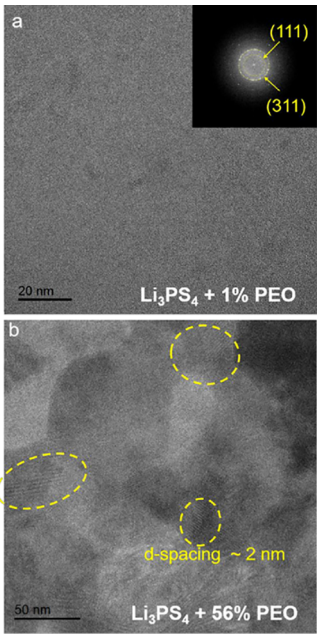

Figure 4. Representative cryo-TEM images of Li_3PS_4 + PEO composites containing (a) 1 wt % PEO and (b) 56 wt % PEO. FFT in (a) highlights specific planes associated with small amounts of crystalline Li_2S. No β-Li_3PS_4 nanocrystalline domains were detected in these composites.

transition temperature of PEO. At higher magnification, individual atoms could not be resolved in the composites; thus, the large fringes (e.g., d-spacing ∼2 nm in Figure 4b) are unlikely to be Moiré interference patterns.

Incorporating polymer binders (e.g., via the in-situ one-pot synthesis route reported here) greatly facilitates the processability of sulfide SEs. As shown in Figure S6 and Table S1, amorphous Li_3PS_4 + PEO films of 10−30 μm thickness can be prepared on Cu foil via doctor blade coatings. The as-cast layers had very high porosity (70%), but dense films with <5 vol % voids were easily obtained by cold-pressing at 530 MPa. These processing studies demonstrate the proof-of-concept for thin SE layers, which are critical for high energy density SSBs, but optimization of the slurry rheology and coating/drying procedures is required to improve adhesion to the substrate (e.g., flaking of SE films was observed after drying, see Figure S6c). Incorporation of fiber reinforcements and hot-pressing may further improve the mechanical properties of the composite SE layers as was recently demonstrated for related systems.[47,48] Ideally the SE layer would be integrated into SSBs by casting directly onto a composite solid-state cathode. However, such studies are beyond the scope of this work, which is primarily focused on evaluating how SE composition and structure impact Li^+ transport properties. As such, Li^+ conductivities were measured with cold-pressed pellets (ca. 0.5−1 mm thick) to draw fundamental structure/function correlations.

The Li^+ conductivities of crystalline β-Li_3PS_4 and amorphous Li_3PS_4 + PEO composites were evaluated through alternating current (AC) impedance measurements on the blocking cell configuration shown in Figure 5a. Nyquist plots of these cells exhibited vertical capacitive tails due to charge accumulation at the electrode/electrolyte interfaces (see Figure 5b). As shown in Figure 5c, the crystalline β-Li_3PS_4 exhibited high Li^+ conductivity (e.g., 1.2 × 10^{-4} S/cm at room

https://dx.doi.org/10.1021/acs.chemmater.0c01990
Chem. Mater. 2020, 32, 8789−8797

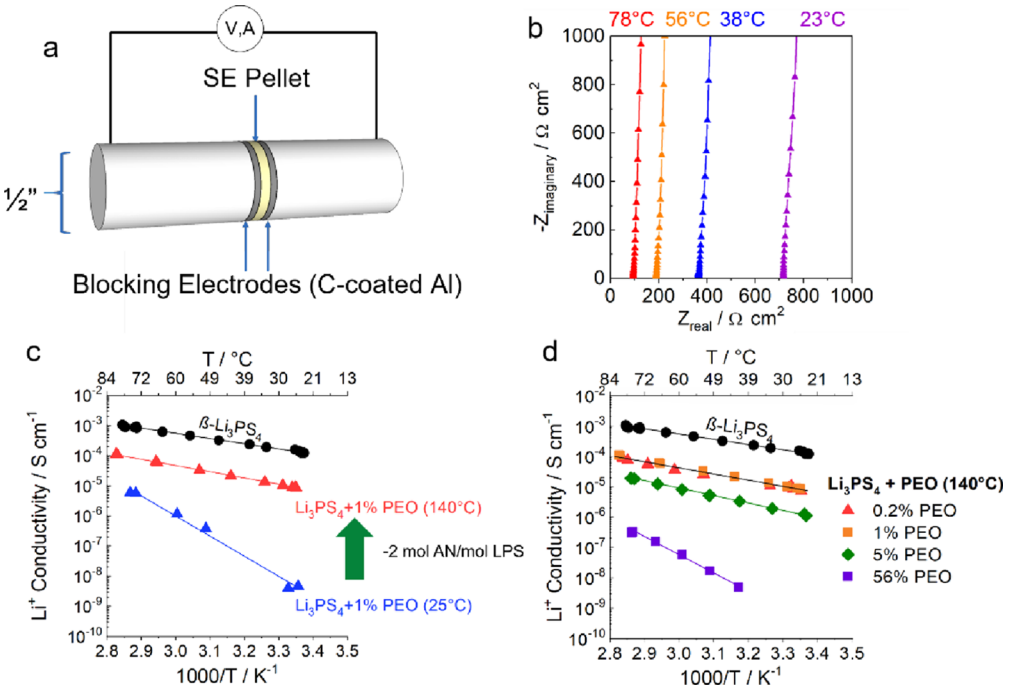

Figure 5. Li^+ conductivity measurements of β-Li_3PS_4 and Li_3PS_4 + PEO composites. (a) Schematic of the electrochemical cell and (b) representative Nyquist plots collected at different temperatures. (c, d) Arrhenius plots showing Li^+ conductivity as a function of temperature for (c) Li_3PS_4 + 1 wt % PEO dried at 25 and 140 °C and (d) Li_3PS_4 + PEO composites containing 0.2−56 wt % PEO. AC perturbations of 500 mV were used for Li_3PS_4 + 1% PEO dried at 25 °C (panel c) and Li_3PS_4 + 56% PEO dried at 140 °C (panel d) because of the high resistance of these samples.

temperature) with an activation energy of 0.36 eV, values which are in good agreement with previous reports.[2,3] In comparison, the ionic conductivity of the polymer/ceramic composites varied greatly depending on the thermal treatment. For instance, after drying under vacuum at 25 °C, the conductivity of Li_3PS_4 + 1% PEO was 5 orders of magnitude lower than that of β-Li_3PS_4 (e.g., 4.5×10^{-9} S/cm at room temperature) due to the presence of coordinated AN. After heating to 140 °C, the material evolved ∼2 mol AN/mol Li_3PS_4 (corresponding to ∼30 wt % loss), and the ionic conductivity increased 3 orders of magnitude at room temperature (i.e., from 4.5×10^{-9} to 8.4×10^{-6} S/cm). The higher conductivity coincided with a lower activation energy (1.37 vs 0.45 eV for samples dried at 25 and 140 °C, respectively), indicating that the coordinated AN hindered Li^+ mobility and provided a less favorable energy landscape for long-range Li^+ migration. The role of different thermal treatments on the composite's microstructure was explored using Raman spectroscopy and XPS as is discussed later in the text.

Figure 5d shows the Li^+ conductivity of Li_3PS_4 + PEO composites heated at 140 °C as a function of the polymer content. Samples with 0.2 and 1 wt % PEO exhibited identical conductivities and activation energies within experimental error, which indicates that small amounts of binder can be incorporated without compromising SE performance. Increasing the PEO content from 1 to 5 wt % slightly decreased the conductivity (e.g., 1.1×10^{-6} S/cm at room temperature) because of the insulating nature of PEO. As expected, a higher PEO loading resulted in even lower conductivity, and the sample with 56 wt % PEO could only be measured at elevated temperatures (e.g., 4.8×10^{-9} S/cm at 42 °C) because of its high resistance. Based on these findings, the polymer content in amorphous Li_3PS_4 + PEO composites should be limited to ca. 1−5 wt % to ensure reasonable ionic conductivity while providing enough binder to facilitate processing.

Compared to the nanocrystalline β-Li_3PS_4, the lower conductivity of the Li_3PS_4 + PEO polymer/ceramic composites is attributed to: (i) the negligible conductivity of the polymer phase, which contains no Li-based salt, (ii) the intrinsic properties of amorphous Li_3PS_4, which may contain Li-P-S bonding environments with lower Li^+ mobility compared to β-Li_3PS_4, and (iii) the lower Li^+ concentration in amorphous Li_3PS_4 as indicated by the presence of trace Li_2S from the XRD and cryo-TEM measurements (Figures 2−4). To better understand the near-order structure of the composites and how it changes with thermal treatment, Raman spectroscopy and XPS measurements were performed on Li_3PS_4 + 1% PEO.

Figure 6 presents the Raman spectra of amorphous composites containing 1% PEO before and after thermal treatments up to 250 °C. When dried at room temperature, the sample showed several Raman-active bands in the range 100−600 cm^{-1} in which various P-S stretches are expected. The bands at 395 and 435 cm^{-1} are assigned to P-S vibrational modes of the $P_2S_6^{2-}$ and PS_4^{3-} polyanions, respectively (Figure 6).[49] The peak at 2920 cm^{-1} is attributed to the C-H stretch of coordinated AN (Figure S5). This C-H stretch was absent from all annealed samples, indicating that the coordinated AN was removed at 140 °C. In comparison, previous studies[3,29] have shown that heat treatments at 200 °C are required to remove coordinated AN from β-Li_3PS_4, which suggests that the solvent is less strongly coordinated to amorphous Li_3PS_4.

The Raman spectra of Li_3PS_4 + 1 wt % PEO exhibited subtle changes in the range 390−430 cm^{-1} upon heating due to rearrangement of the polyanionic network. More specifically, heating at 140−200 °C resulted in a new band at 408 cm^{-1}

https://dx.doi.org/10.1021/acs.chemmater.0c01990
Chem. Mater. 2020, 32, 8789−8797

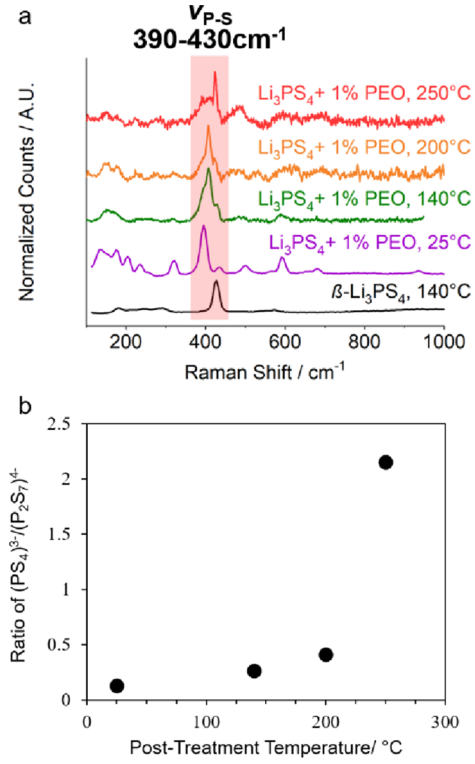

Figure 6. (a) Raman spectra of β-Li_3PS_4 and Li_3PS_4 + 1 wt % PEO dried overnight at 25−250 °C and (b) qualitative ratio of PS_4^{3-}/$P_2S_7^{4-}$in the Li_3PS_4 + 1 wt % PEO composites with different post-treatment temperatures as determined by the relative peak intensities at 408 and 430 cm^{-1}. After thermal annealing at 140−200 °C, the amorphous Li_3PS_4 underwent structural rearrangements to form a more ionically conductive polyanionic network.

(attributed to formation of $P_2S_7^{4-}$ polyanions) and increased intensity ~430 cm^{-1} (attributed to PS_4^{3-}).[50] The relative ratio of PS_4^{3-} and $P_2S_7^{4-}$ after different thermal treatments was qualitatively estimated based on the relative peak intensities at 408 and 430 cm^{-1} as shown in Figure 6b. Compounds with these polyanionic structures (e.g., Li_3PS_4 and $Li_7P_3S_{11}$) typically exhibit higher Li^+ conductivity compared to structures containing $P_2S_6^{2-}$ (e.g., $Li_2P_2S_6$), which was the predominant moiety in the unheated sample.[51] Further heating to 250 °C caused thermal decomposition of the Li_3PS_4 + PEO composite as evidenced by the appearance of a broad band ~1300 cm^{-1} (see Figure S5), which is attributed to a disordered carbonaceous product. The only possible carbon sources in the precursors are PEO and AN. As such, the sulfide phase likely reacted with either the PEO or trace amounts of coordinated solvent at temperatures >200 °C. The decomposition products are amorphous as evidenced by the lack of crystalline phases after annealing (see XRD results in Figure 2).

Collectively, the Raman results shown in Figure 6 and Figure S5 indicate that the composites' higher Li^+ conductivity after annealing at 140 °C was due to (i) removal of coordinated AN and (ii) reorganization of the amorphous structure to form a more ionically conductive polyanionic framework. Future studies should aim to further increase the ionic conductivity of these materials by: (i) optimizing the Li_2S/P_2S_5 molar ratio to eliminate Li_2S impurities, (ii) incorporating Li-based salts in the PEO binder matrix, and (iii) utilizing one-pot synthesis routes with different solvents and binders that do not inhibit crystallization of β-Li_3PS_4.

To complement the Raman measurements shown in Figure 6, the near-surface structures of Li_3PS_4 + 1% PEO and β-Li_3PS_4 were studied using XPS, and core-level S 2p, P 2p, and Li 1s spectra are shown in Figure 7a−c, respectively. The S 2p and P

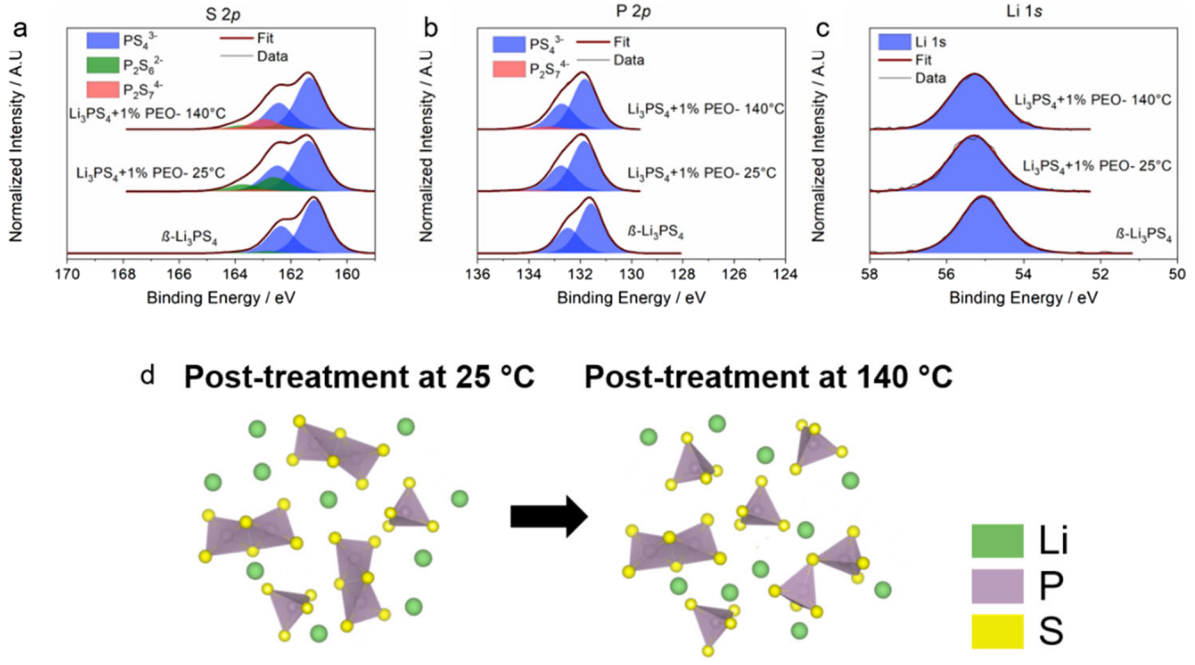

Figure 7. XPS analysis showing core-level scans of (a) S 2p, (b) P 2p, and (c) Li 1s for β-Li_3PS_4 and Li_3PS_4 + 1 wt % PEO dried overnight at 25 and 140 °C. Compared to β-Li_3PS_4, the amorphous composites contained a broad distribution of Li-P-S bonding environments, which resulted in lower Li^+ conductivity (shown in Figure 5c and d). (d) Schematic of the structural variation schematic showing the structural variation of amorphous Li_3PS_4 as a function of postprocessing temperature as a function of postprocessing temperature.

https://dx.doi.org/10.1021/acs.chemmater.0c01990
Chem. Mater. 2020, 32, 8789−8797

2p spectra of β-Li_3PS_4 showed doublets due to $2p_{1/2}$ and $2p_{3/2}$ spin-orbit splitting where the components were separated by 1.1 and 0.9 eV for S 2p and P 2p, respectively. These features are consistent with previous reports[52,53] and indicate that a single type of P-S bonding environment was present in β-Li_3PS_4 (i.e., isolated PS_4^{3-} tetrahedra). In comparison, the amorphous Li_3PS_4 + 1% PEO samples showed a significantly broader signal in the S 2p spectra with additional features at 162.6−163.7 eV which are assigned to $P_2S_6^{2-}$ and $P_2S_7^{4-}$ polyanion structures that contain bridging S bonds.[50,54] Notably, the sample annealed at 140 °C contained more $P_2S_7^{4-}$ and less $P_2S_6^{2-}$ compared to the unheated sample, which is consistent with the Raman findings shown in Figure 6. On the other hand, the P 2p spectra of the composites were very similar to that of the β-Li_3PS_4, which may be due to similar 2p binding energies of phosphorus in different polyanion structures (e.g., PS_4^{3-} vs $P_2S_7^{4-}$), thus making it difficult to resolve these subunits.[50] The Li 1s spectra of the composites were broader and shifted by +0.2 eV compared to β-Li_3PS_4, indicating that the amorphous Li_3PS_4 contained a wider distribution of local Li-P-S bonding environments which led to their lower Li^+ conductivity. The XPS and Raman data show important transformations in the PS_4^{3-}, $P_2S_6^{2-}$, and $P_2S_7^{4-}$ polyanions during annealing, which are presented schematically in Figure 7d. These structural variations have critical implications on the electrochemical performance of the composite SEs.

A Li|Li_3PS_4 + 1%PEO|Li symmetric cell was constructed to assess the (electro)chemical compatibility of the SE with Li metal. Figure 8a shows the performance of the cell cycled at

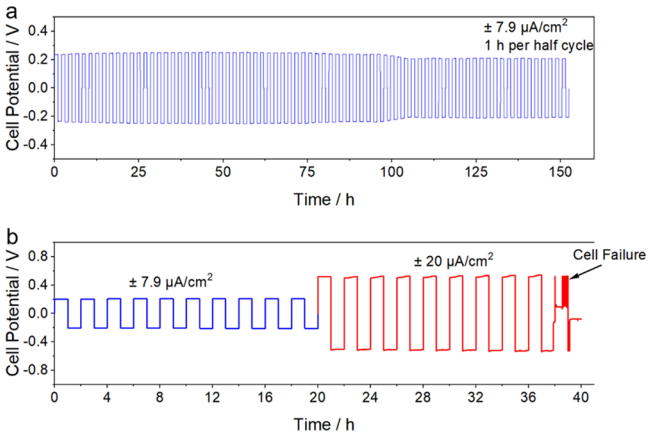

Figure 8. Electrochemical results for electrochemical results for a Li|Li_3PS_4+1%PEO|Li symmetric cell cycled galvanostatically at: (a) 7.9 $\mu A/cm^2$ over 150 h and (b) 7.9−20 $\mu A/cm^2$ until failure. Li_3PS_4 + 1% PEO powder was annealed at 140 °C under vacuum prior to cell assembly and testing.

7.9 $\mu A/cm^2$ at room temperature. During initial cycles, the cell overpotential was ca. 0.24 V (corresponding to an effective SE conductivity of 2×10^{-6} S/cm) and decreased by ~12% after 100 h, possibly due to improved Li wetting at the interface. Notably, the cell exhibited stable cycling performance over 150 h at low current density, which indicates that the composite SE formed a kinetically stabilized passive film at the Li/SE interface. When cycled at 20 $\mu A/cm^2$, the cell shorted after 10 cycles (1 h per half cycle) because of unstable Li growth. Although amorphous/glassy SEs lack a discrete grain structure, Li may preferentially grow along defects (e.g., between discrete particles in cold-pressed pellets or along artificial Lipon-Lipon interfaces as was recently demonstrated by Westover et al.[9]), and new processing methods (e.g., hot-pressing) are needed to eliminate such defects in SE layers prepared from amorphous powders.

CONCLUSIONS

At present, SSBs are challenged by two major bottlenecks, being (i) the lack of scalable processing methods to produce thin SE layers and (ii) unstable Li growth during battery operation due to nonuniform current densities across the SE/Li interface. Here, one strategy is to consider new types of amorphous Li^+ conductors, understand how their local structure influences Li^+ transport, and explore cost-effective manufacturing routes.

This work describes the development of a new class of polymer/ceramic composite SEs containing amorphous Li_3PS_4. To address processing difficulties encountered with β-Li_3PS_4, these materials are synthesized in situ with a PEO binder/network former using a one-pot solvent-mediated route. The structure of Li_3PS_4 was highly dependent on the solvent and thermal processing conditions. The polymer's crystallinity was largely suppressed in the composites, indicating a strong coordination between the polymer's ether group and the amorphous Li_3PS_4.

The ionic conductivity of amorphous Li_3PS_4 + PEO composites increased several orders of magnitude (e.g., up to 1.1×10^{-4} S/cm at 80 °C) after heating at 140 °C due to (i) removal of coordinated AN and (ii) rearrangement of the amorphous structure to form a more ionically conductive polyanionic network. Raman spectroscopy and XPS measurements indicate that thermal annealing increased the amount of $P_2S_7^{4-}$ and PS_4^{3-} units to promote higher Li^+ conductivity. Overall, the solvent-mediated synthesis approach developed here can be applied to a wide range of composite sulfide-based SEs where the material structure and electrochemical properties can be tuned by modifying key processing variables (e.g., solvent, mixing protocol, and thermal post-treatment).

EXPERIMENTAL METHODS

Synthesis of Li_3PS_4 + PEO Composites. Amorphous Li_3PS_4-based SEs were prepared by dispersing Li_2S (Sigma-Aldrich), P_2S_5 (Sigma-Aldrich), and PEO (600 kDa, Sigma-Aldrich) in AN (anhydrous, Sigma-Aldrich). The composites contained Li_2S and P_2S_5 in a 3/1 molar ratio, and the PEO content ranged from 0−56 wt %. The dispersions were sealed in HDPE vials containing ZrO_2 milling media and blended on a Turbula Model T2F shaker-mixer for several hours to obtain homogenous slurries. The samples were subsequently dried under vacuum at 25−45 °C to remove excess solvent, and the resulting powders were annealed at temperatures up to 250 °C for at least 12 h. For comparison, crystalline β-Li_3PS_4 was prepared by blending Li_2S and P_2S_5 in a 3/1 molar ratio in THF (Sigma-Aldrich) followed by drying at 140 °C under vacuum overnight. Slurry cast SE films were prepared by dispersing amorphous Li_3PS_4 + 5 wt % PEO in AN (18 wt % solids) and blending on the Turbula shaker-mixer for 1 h. The slurry was cast onto Cu foil (15 μm thick) using an 8 mil doctor blade and dried overnight under vacuum at room temperature. All syntheses, processing, and characterization were performed under an Ar atmosphere to mitigate air exposure.

XPS. The powder samples were dispersed onto double-sided tape fixed to clean glass slides and placed in a vacuum transfer holder inside an Ar-filled glovebox. The holder was evacuated and sealed in the glovebox load-lock before transferring to the XPS instrument (Thermo Scientific Model K-Alpha XPS), which contained a

https://dx.doi.org/10.1021/acs.chemmater.0c01990
Chem. Mater. 2020, 32, 8789−8797

monochromated, microfocusing Al Kα X-ray source (1486.6 eV) with a variable X-ray spot size (30−400 μm). This work used a 400 μm X-ray spot size to maximize the signal intensity and to obtain an average surface composition over a large area. The instrument used a hemispherical electron energy analyzer equipped with a 128 multichannel detector system. The base pressure in the analysis chamber was 3×10^{-10} mbar. Wide energy range survey spectra (0−1350 eV) were acquired for qualitative and quantitative analysis using a pass energy setting of 200 eV. To assess the chemical bonding of identified elements, narrow energy range core level spectra were acquired with a pass energy setting of 50 eV. Data were collected and processed using the Thermo Scientific Avantage XPS software package (v 4.61). Spectra were charge corrected using the C 1s core level peak set to 284.8 eV.

Electrochemical Characterization. The ionic conductivities of β-Li_3PS_4 and Li_3PS_4/PEO composite SE pellets were measured in symmetric cells containing carbon-coated Al blocking electrodes. To prepare these cells, the SE powder was compacted at 500 MPa for 1 min at room temperature in a 13 mm pellet die using a hydraulic press. Carbon-coated Al disks (1/2″ diameter) were placed on both sides of the sample prior to pellet pressing. The ejected pellet (ca. 0.5−1 mm thick) was sandwiched between stainless steel rods (1/2″ diameter), and heat shrink was applied to ensure concentric alignment of cell components. AC impedance spectra of the cells were acquired at 25−80 °C at open-circuit using a 10 mV AC perturbation (unless indicated otherwise) over a frequency range of 1×10^6−0.5 Hz using a Bio-Logic SP-200 potentiostat/galvanostat. The total ionic conductivity (σ_{Li^+}, S/cm) was calculated at 25−80 °C using eq 1:

$$\sigma_{Li^+} = \frac{x}{R \times A} \quad (1)$$

where x is the pellet thickness (cm), R is the x-axis intercept from the Nyquist plots (Ω), and A is the electrode area (cm^2). For graphical clarity, conductivity data were reported as $\log(\sigma_{Li+})$ versus $1000/T$, but activation energies (E_a, eV) were calculated using the following relationship:

$$\sigma_{Li^+}T = Ae^{-E_a/R\times T} \quad (2)$$

where A is a constant (S K cm^{-1}) and R is the universal gas constant (eV K^{-1}). Cells were thermally cycled at least 2 times to ensure reproducible conductivity measurements. Electrochemical measurements were performed inside an Ar-filled glovebox.

A Li|Li_3PS_4 + 1%PEO|Li symmetric cell was prepared by attaching Li electrodes (1/2″ diameter, approximately 45 μm thick on Cu foil) to both sides of the SE pellet (amorphous Li_3PS_4 + 1%PEO annealed at 140 °C). The Cu|Li|Li_3PS_4 + 1%PEO|Li|Cu ensemble was sandwiched between stainless steel rods (1/2″ diameter), and heat shrink was applied to ensure concentric alignment of cell components. The cell was cycled at current densities of 7.9−20 μA/cm^2 (1 h per half cycle) at room temperature inside an Ar-filled glovebox.

Raman Spectroscopy. Raman spectra were acquired with an Alpha 300 confocal Raman microscope (WITec, GmbH) using a solid-state 532 nm excitation laser, a 20 × objective lens, and a grating with 600 grooves per mm. The laser spot size and power were approximately 1 μm and 100 μW, respectively. Representative Raman spectra were analyzed using WITec Project Plus software. Powder samples were hermetically sealed in an optical cell (EL-Cell) in an Ar-filled glovebox prior to Raman measurements to avoid air exposure.

XRD. XRD measurements were performed on a Scintag XDS 2000 powder diffractometer with Cu Kα radiation (λ = 1.5406 Å) in the 2θ range of 10−80 °. The operating voltage and current of the X-ray generator were 38 kV and 32−35 mA, respectively. Powders were mounted on glass slides and covered with Kapton tape to mitigate air exposure during XRD measurements.

Electron Microscopy. The morphology and elemental composition of Li_3PS_4/PEO pellets were assessed using SEM and EDS (Bruker) with a Zeiss Merlin SEM using an acceleration voltage of 1−20 kV. Samples were loaded in a vacuum-tight sample stage described previously[55] to avoid air exposure during sample transfer.

Samples for cryo-TEM were prepared by drop-casting Li_3PS_4/PEO powders dispersed in AN onto lacey carbon TEM grids inside an Ar-filled glovebox. Specimens were exposed to ambient conditions for ca. 3 min during sample loading. Cryo-TEM measurements were conducted on an aberration-corrected FEI Titan (scanning) transmission electron microscope (S/TEM) operated at 300 kV using a Gatan Cryo Transfer holder cooled by liquid nitrogen. During TEM operation, the spatial resolution was ~0.63 Å, and the electron dose flux was <1000 e^- $Å^{-2}$ s^{-1}. All images were analyzed using Digital Micrograph software (Gatan).

■ ASSOCIATED CONTENT

Supporting Information

The Supporting Information is available free of charge at https://pubs.acs.org/doi/10.1021/acs.chemmater.0c01990.

XRD patterns; Raman spectra; SEM/EDX images; slurry casting studies (PDF)

■ AUTHOR INFORMATION

Corresponding Authors

Ethan C. Self − *Chemical Sciences Division, Oak Ridge National Laboratory, Oak Ridge, Tennessee 37831, United States;* orcid.org/0000-0001-6006-6317; Email: selfec@ornl.gov

Zachary D. Hood − *Department of Materials Science and Engineering, Massachusetts Institute of Technology, Cambridge, Massachusetts 02139, United States;* orcid.org/0000-0002-5720-4392; Email: zhood@mit.edu

Jagjit Nanda − *Chemical Sciences Division, Oak Ridge National Laboratory, Oak Ridge, Tennessee 37831, United States;* orcid.org/0000-0002-6875-0057; Email: nandaj@ornl.gov

Authors

Teerth Brahmbhatt − *The Bredesen Center for Interdisciplinary Research and Graduate Education, The University of Tennessee, Knoxville, Tennessee 37996, United States*

Frank M. Delnick − *Chemical Sciences Division, Oak Ridge National Laboratory, Oak Ridge, Tennessee 37831, United States*

Harry M. Meyer, III − *Center for Nanophase Material Sciences, Oak Ridge National Laboratory, Oak Ridge, Tennessee 37831, United States*

Guang Yang − *Chemical Sciences Division, Oak Ridge National Laboratory, Oak Ridge, Tennessee 37831, United States;* orcid.org/0000-0003-0583-6272

Jennifer L. M. Rupp − *Department of Materials Science and Engineering and Department of Electrical Engineering and Computer Science, Massachusetts Institute of Technology, Cambridge, Massachusetts 02139, United States;* orcid.org/0000-0001-7160-0108

Complete contact information is available at: https://pubs.acs.org/10.1021/acs.chemmater.0c01990

Author Contributions

#E.C.S. and Z.D.H. contributed equally. E.C.S. and Z.D.H. designed and executed experiments, prepared figures, and wrote the manuscript. T.B. and F.M.D. synthesized the solid electrolytes and measured their ionic conductivity. H.M.M. III performed XPS measurements and analysis. G.Y. provided insights into the Raman spectroscopy and XPS results. J.N. and J.L.M.R. assisted with data interpretation and manuscript writing. J.N. led and guided the project. The manuscript was written through contributions of all authors. All authors have given approval to the final version of the manuscript.

https://dx.doi.org/10.1021/acs.chemmater.0c01990
Chem. Mater. 2020, 32, 8789−8797

Notes

The authors declare no competing financial interest.

■ ACKNOWLEDGMENTS

The authors thank Dr. Jianping Zheng and Dr. Annadanesh Shellikeri for supplying the thin Li foil used in the Li|SE|Li symmetric cells. This research was conducted at Oak Ridge National Laboratory, managed by UT Battelle, LLC, for the U.S. Department of Energy (DOE) and is supported by Asst. Secretary, Energy Efficiency and Renewable Energy (EERE), Vehicle Technologies Office (VTO) through the Advanced Battery Materials Research (BMR) Program. Electron microscopy and energy-dispersive X-ray spectroscopy studies were conducted at the Center for Nanophase Materials Sciences (CNMS), which is a DOE Office of Science User Facility. This manuscript has been authored in part by UT-Battelle, LLC, under contract DE-AC05-00OR22725 with the US Department of Energy (DOE). The publisher, by accepting the article for publication, acknowledges that the US government retains a nonexclusive, paid-up, irrevocable, worldwide license to publish or reproduce the published form of this manuscript, or allow others to do so, for US government purposes. DOE will provide public access to these results of federally sponsored research in accordance with the DOE Public Access Plan (http://energy.gov/downloads/doe-public-access-plan).

■ REFERENCES

(1) Liu, Q.; Geng, Z.; Han, C.; Fu, Y.; Li, S.; He, Y.-b.; Kang, F.; Li, B. Challenges and perspectives of garnet solid electrolytes for all solid-state lithium batteries. *J. Power Sources* **2018**, *389*, 120−134.

(2) Liu, Z.; Fu, W.; Payzant, E. A.; Yu, X.; Wu, Z.; Dudney, N. J.; Kiggans, J.; Hong, K.; Rondinone, A. J.; Liang, C. Anomalous high ionic conductivity of nanoporous beta-Li3PS4. *J. Am. Chem. Soc.* **2013**, *135*, 975−978.

(3) Wang, H.; Hood, Z. D.; Xia, Y.; Liang, C. Fabrication of ultrathin solid electrolyte membranes of β-Li3PS4 nanoflakes by evaporation-induced self-assembly for all-solid-state batteries. *J. Mater. Chem. A* **2016**, *4*, 8091−8096.

(4) Hood, Z. D.; Wang, H.; Pandian, A. S.; Peng, R.; Gilroy, K. D.; Chi, M.; Liang, C.; Xia, Y. Fabrication of Sub-Micrometer-Thick Solid Electrolyte Membranes of β-Li3PS4 via Tiled Assembly of Nanoscale, Plate-Like Building Blocks. *Adv. Energy Mater.* **2018**, *8*, 1800014.

(5) Lewis, J. A.; Tippens, J.; Cortes, F. J. Q.; McDowell, M. T. Chemo-Mechanical Challenges in Solid-State Batteries. *Trendsin Chem.* **2019**, *1*, 845−857.

(6) Frenck, L.; Sethi, G. K.; Maslyn, J. A.; Balsara, N. P. Factors That Control the Formation of Dendrites and Other Morphologies on Lithium Metal Anodes. *Front. in Energ. Res.* **2019**, *7*, 115.

(7) Porz, L.; Swamy, T.; Sheldon, B. W.; Rettenwander, D.; Frömling, T.; Thaman, H. L.; Berendts, S.; Uecker, R.; Carter, W. C.; Chiang, Y.-M. Mechanism of Lithium Metal Penetration through Inorganic Solid Electrolytes. *Adv. Energy Mater.* **2017**, *7*, 1701003.

(8) Shen, Y.; Zhang, Y.; Han, S.; Wang, J.; Peng, Z.; Chen, L. Unlocking the Energy Capabilities of Lithium Metal Electrode with Solid-State Electrolytes. *Joule* **2018**, *2*, 1674−1689.

(9) Westover, A. S.; Dudney, N. J.; Sacci, R. L.; Kalnaus, S. Deposition and Confinement of Li Metal along an Artificial Lipon−Lipon Interface. *ACS Energy Lett.* **2019**, *4*, 651−655.

(10) Garbayo, I.; Struzik, M.; Bowman, W. J.; Pfenninger, R.; Stilp, E.; Rupp, J. L. M. Glass-Type Polyamorphism in Li-Garnet Thin Film Solid State Battery Conductors. *Adv. Energy Mater.* **2018**, *8*, 1702265.

(11) Pfenninger, R.; Struzik, M.; Garbayo, I.; Stilp, E.; Rupp, J. L. M. A low ride on processing temperature for fast lithium conduction in garnet solid-state battery films. *Nat. Energy* **2019**, *4*, 475−483.

(12) Ghidiu, M.; Ruhl, J.; Culver, S. P.; Zeier, W. G. Solution-based synthesis of lithium thiophosphate superionic conductors for solid-state batteries: a chemistry perspective. *J. Mater. Chem. A* **2019**, *7*, 17735−17753.

(13) Miura, A.; Rosero-Navarro, N. C.; Sakuda, A.; Tadanaga, K.; Phuc, N. H. H.; Matsuda, A.; Machida, N.; Hayashi, A.; Tatsumisago, M. Liquid-phase syntheses of sulfide electrolytes for all-solid-state lithium battery. *Nat. Rev. Chem.* **2019**, *3*, 189−198.

(14) Chen, S.; Xie, D.; Liu, G.; Mwizerwa, J. P.; Zhang, Q.; Zhao, Y.; Xu, X.; Yao, X. Sulfide solid electrolytes for all-solid-state lithium batteries: Structure, conductivity, stability and application. *Energy Storage Materials* **2018**, *14*, 58−74.

(15) Lau, J.; DeBlock, R. H.; Butts, D. M.; Ashby, D. S.; Choi, C. S.; Dunn, B. S. Sulfide Solid Electrolytes for Lithium Battery Applications. *Adv. Energy Mater.* **2018**, *8*, 1800933.

(16) Calpa, M.; Rosero-Navarro, N. C.; Miura, A.; Tadanaga, K. Instantaneous preparation of high lithium-ion conducting sulfide solid electrolyte Li7P3S11 by a liquid phase process. *RSC Adv.* **2017**, *7*, 46499−46504.

(17) Yubuchi, S.; Teragawa, S.; Aso, K.; Tadanaga, K.; Hayashi, A.; Tatsumisago, M. Preparation of high lithium-ion conducting Li6PS5Cl solid electrolyte from ethanol solution for all-solid-state lithium batteries. *J. Power Sources* **2015**, *293*, 941−945.

(18) Chida, S.; Miura, A.; Rosero-Navarro, N. C.; Higuchi, M.; Phuc, N. H. H.; Muto, H.; Matsuda, A.; Tadanaga, K. Liquid-phase synthesis of Li6PS5Br using ultrasonication and application to cathode composite electrodes in all-solid-state batteries. *Ceram. Int.* **2018**, *44*, 742−746.

(19) Park, K. H.; Oh, D. Y.; Choi, Y. E.; Nam, Y. J.; Han, L.; Kim, J. Y.; Xin, H.; Lin, F.; Oh, S. M.; Jung, Y. S. Solution-Processable Glass LiI-Li4 SnS4 Superionic Conductors for All-Solid-State Li-Ion Batteries. *Adv. Mater.* **2016**, *28*, 1874−1883.

(20) Wu, F.; Fitzhugh, W.; Ye, L.; Ning, J.; Li, X. Advanced sulfide solid electrolyte by core-shell structural design. *Nat. Commun.* **2018**, *9*, 4037.

(21) Xu, J.; Liu, L.; Yao, N.; Wu, F.; Li, H.; Chen, L. Liquid-involved synthesis and processing of sulfide-based solid electrolytes, electrodes, and all-solid-state batteries. *Materials Today Nano* **2019**, *8*, 100048.

(22) Wang, Y.; Richards, W. D.; Ong, S. P.; Miara, L. J.; Kim, J. C.; Mo, Y.; Ceder, G. Design principles for solid-state lithium superionic conductors. *Nat. Mater.* **2015**, *14*, 1026−1031.

(23) Yang, Y.; Wu, Q.; Cui, Y.; Chen, Y.; Shi, S.; Wang, R. Z.; Yan, H. Elastic Properties, Defect Thermodynamics, Electrochemical Window, Phase Stability, and Li(+) Mobility of Li3PS4: Insights from First-Principles Calculations. *ACS Appl. Mater. Interfaces* **2016**, *8*, 25229−25242.

(24) Lepley, N. D.; Holzwarth, N. A. W.; Du, Y. A. Structures, Li+ mobilities, and interfacial properties of solid electrolytes Li3PS4 and Li3PO4 from first principles. *Phys. Rev. B* **2013**, *88*, 104103.

(25) Baba, T.; Kawamura, Y. Structure and Ionic Conductivity of Li2S−P2S5 Glass Electrolytes Simulated with First-Principles Molecular Dynamics. *Front.Energy Res* **2016**, *4*, 22.

(26) Judez, X.; Eshetu, G. G.; Li, C.; Rodriguez-Martinez, L. M.; Zhang, H.; Armand, M. Opportunities for Rechargeable Solid-State Batteries Based on Li-Intercalation Cathodes. *Joule* **2018**, *2*, 2208−2224.

(27) Aetukuri, N. B.; Kitajima, S.; Jung, E.; Thompson, L. E.; Virwani, K.; Reich, M.-L.; Kunze, M.; Schneider, M.; Schmidbauer, W.; Wilcke, W. W.; Bethune, D. S.; Scott, J. C.; Miller, R. D.; Kim, H.-C. Flexible Ion-Conducting Composite Membranes for Lithium Batteries. *Adv. Energy Mater.* **2015**, *5*, 1500265.

(28) Xu, R.; Yue, J.; Liu, S.; Tu, J.; Han, F.; Liu, P.; Wang, C. Cathode-Supported All-Solid-State Lithium−Sulfur Batteries with High Cell-Level Energy Density. *ACS Energy Lett.* **2019**, *4*, 1073−1079.

(29) Chen, S.; Wang, J.; Zhang, Z.; Wu, L.; Yao, L.; Wei, Z.; Deng, Y.; Xie, D.; Yao, X.; Xu, X. In-situ preparation of poly(ethylene oxide)/Li3PS4 hybrid polymer electrolyte with good nanofiller

https://dx.doi.org/10.1021/acs.chemmater.0c01990
Chem. Mater. 2020, 32, 8789−8797

distribution for rechargeable solid-state lithium batteries. *J. Power Sources* **2018**, *387*, 72−80.
(30) Chen, B.; Huang, Z.; Chen, X.; Zhao, Y.; Xu, Q.; Long, P.; Chen, S.; Xu, X. A new composite solid electrolyte PEO/Li10GeP2S12/SN for all-solid-state lithium battery. *Electrochim. Acta* **2016**, *210*, 905−914.
(31) Chen, X. C.; Liu, X.; Samuthira Pandian, A.; Lou, K.; Delnick, F. M.; Dudney, N. J. Determining and Minimizing Resistance for Ion Transport at the Polymer/Ceramic Electrolyte Interface. *ACS Energy Lett.* **2019**, *4*, 1080−1085.
(32) Pandian, A. S.; Chen, X. C.; Chen, J.; Lokitz, B. S.; Ruther, R. E.; Yang, G.; Lou, K.; Nanda, J.; Delnick, F. M.; Dudney, N. J. Facile and scalable fabrication of polymer-ceramic composite electrolyte with high ceramic loadings. *J. Power Sources* **2018**, *390*, 153−164.
(33) Li, J.; Zhu, K.; Yao, Z.; Qian, G.; Zhang, J.; Yan, K.; Wang, J. A promising composite solid electrolyte incorporating LLZO into PEO/PVDF matrix for all-solid-state lithium-ion batteries. *Ionics* **2020**, *26*, 1101−1108.
(34) Gupta, A.; Sakamoto, J. Controlling Ionic Transport through the PEO-LiTFSI/LLZTO Interface. *Electrochem. Soc. Interface* **2019**, *28*, 63−69.
(35) Cai, D.; Wang, D.; Chen, Y.; Zhang, S.; Wang, X.; Xia, X.; Tu, J. A highly ion-conductive three-dimensional LLZAO-PEO/LiTFSI solid electrolyte for high-performance solid-state batteries. *Chem. Eng. J.* **2020**, *394*, 124993.
(36) Liu, S.; Shan, H.; Xia, S.; Yan, J.; Yu, J.; Ding, B. Polymer Template Synthesis of Flexible SiO2 Nanofibers to Upgrade Composite Electrolytes. *ACS Appl. Mater. Interfaces* **2020**, *12*, 31439−31447.
(37) Zhang, W.; Wang, X.; Zhang, Q.; Wang, L.; Xu, Z.; Li, Y.; Huang, S. Li7La3Zr2O12 Ceramic Nanofiber-Incorporated Solid Polymer Electrolytes for Flexible Lithium Batteries. *ACS Appl. Energy Mater.* **2020**, *3*, 5238−5246.
(38) Zhao, C. Z.; Zhang, X. Q.; Cheng, X. B.; Zhang, R.; Xu, R.; Chen, P. Y.; Peng, H. J.; Huang, J. Q.; Zhang, Q. An anion-immobilized composite electrolyte for dendrite-free lithium metal anodes. *Proc. Natl. Acad. Sci. U. S. A.* **2017**, *114*, 11069−11074.
(39) Hu, J.; Wang, W.; Yu, R.; Guo, M.; He, C.; Xie, X.; Peng, H.; Xue, Z. Solid polymer electrolyte based on ionic bond or covalent bond functionalized silica nanoparticles. *RSC Adv.* **2017**, *7*, 54986−54994.
(40) Yao, P.; Yu, H.; Ding, Z.; Liu, Y.; Lu, J.; Lavorgna, M.; Wu, J.; Liu, X. Review on Polymer-Based Composite Electrolytes for Lithium Batteries. *Front Chem* **2019**, *7*, 522.
(41) Lv, F.; Wang, Z.; Shi, L.; Zhu, J.; Edström, K.; Mindemark, J.; Yuan, S. Challenges and development of composite solid-state electrolytes for high-performance lithium ion batteries. *J. Power Sources* **2019**, *441*, 227175.
(42) Chen, X.; Vereecken, P. M. Solid and Solid-Like Composite Electrolyte for Lithium Ion Batteries: Engineering the Ion Conductivity at Interfaces. *Adv. Mater. Interfaces* **2018**, *6*, 1800899.
(43) Wang, Y.; Lu, D.; Bowden, M.; El Khoury, P. Z.; Han, K. S.; Deng, Z. D.; Xiao, J.; Zhang, J.-G.; Liu, J. Mechanism of Formation of Li7P3S11 Solid Electrolytes through Liquid Phase Synthesis. *Chem. Mater.* **2018**, *30*, 990−997.
(44) Tong, Y.; Lin, Y.; Wang, S.; Song, M. A study of crystallisation of poly (ethylene oxide) and polypropylene on graphene surface. *Polymer* **2015**, *73*, 52−61.
(45) Wang, X.; Li, Y.; Meng, Y. S. Cryogenic Electron Microscopy for Characterizing and Diagnosing Batteries. *Joule* **2018**, *2*, 2225−2234.
(46) Hood, Z. D.; Chi, M. Mechanistic understanding and strategies to design interfaces of solid electrolytes: insights gained from transmission electron microscopy. *J. Mater. Sci.* **2019**, *54*, 10571−10594.
(47) Yersak, T.; Salvador, J. R.; Schmidt, R. D.; Cai, M. Hot Pressed, Fiber-Reinforced (Li2S)70(P2S5)30 Solid-State Electrolyte Separators for Li Metal Batteries. *ACS Appl. Energy Mater.* **2019**, *2*, 3523−3531.
(48) Yersak, T.; Salvador, J. R.; Schmidt, R. D.; Cai, M. Hybrid Li-S pouch cell with a reinforced sulfide glass solid-state electrolyte film separator. *Int. J.. Appl. Glass Sci.* **2020**, *00*, 1−11.
(49) Dietrich, C.; Weber, D. A.; Culver, S.; Senyshyn, A.; Sedlmaier, S. J.; Indris, S.; Janek, J.; Zeier, W. G. Synthesis, Structural Characterization, and Lithium Ion Conductivity of the Lithium Thiophosphate Li2P2S6. *Inorg. Chem.* **2017**, *56*, 6681−6687.
(50) Wang, Y.; Matsuyama, T.; Deguchi, M.; Hayashi, A.; Nakao, A.; Tatsumisago, M. X-ray photoelectron spectroscopy for sulfide glass electrolytes in the systems Li2S-P2S5 and Li2S-P2S5-LiBr. *J. Ceram. Soc. Jpn.* **2016**, *124*, 597−601.
(51) Dietrich, C.; Weber, D. A.; Sedlmaier, S. J.; Indris, S.; Culver, S. P.; Walter, D.; Janek, J.; Zeier, W. G. Lithium ion conductivity in Li2S−P2S5 glasses − building units and local structure evolution during the crystallization of superionic conductors Li3PS4, Li7P3S11 and Li4P2S7. *J. Mater. Chem. A* **2017**, *5*, 18111−18119.
(52) Sang, L.; Haasch, R. T.; Gewirth, A. A.; Nuzzo, R. G. Evolution at the Solid Electrolyte/Gold Electrode Interface during Lithium Deposition and Stripping. *Chem. Mater.* **2017**, *29*, 3029−3037.
(53) Kato, A.; Kowada, H.; Deguchi, M.; Hotehama, C.; Hayashi, A.; Tatsumisago, M. XPS and SEM analysis between Li/Li3PS4 interface with Au thin film for all-solid-state lithium batteries. *Solid State Ionics* **2018**, *322*, 1−4.
(54) Dietrich, C.; Koerver, R.; Gaultois, M. W.; Kieslich, G.; Cibin, G.; Janek, J.; Zeier, W. G. Spectroscopic characterization of lithium thiophosphates by XPS and XAS - a model to help monitor interfacial reactions in all-solid-state batteries. *Phys. Chem. Chem. Phys.* **2018**, *20*, 20088−20095.
(55) Howe, J. Y.; Boatner, L. A.; Kolopus, J. A.; Walker, L. R.; Liang, C.; Dudney, N. J.; Schaich, C. R. Vacuum-tight sample transfer stage for a scanning electron microscopic study of stabilized lithium metal particles. *J. Mater. Sci.* **2011**, *47*, 1572−1577.

https://dx.doi.org/10.1021/acs.chemmater.0c01990
Chem. Mater. 2020, 32, 8789−8797